RESEARCH ARTICLE

Effects of ion type and concentration on the structure and aggregation of the amyloid peptide Aβ_{16-22}

Eva Smorodina[1,2] | Batuhan Kav[1] | Hebah Fatafta[1,3] | Birgit Strodel[1,3]

[1]Institute of Biological Information Processing: Structural Biochemistry, Forschungszentrum Jülich, Jülich, Germany

[2]Department of Immunology, University of Oslo and Oslo University Hospital, Oslo, Norway

[3]Institute of Theoretical and Computational Chemistry, Heinrich Heine University Düsseldorf, Düsseldorf, Germany

Correspondence
Birgit Strodel, Institute of Biological Information Processing: Structural Biochemistry, Forschungszentrum Jülich, 52425 Jülich, Germany.
Email: b.strodel@fz-juelich.de

Abstract

Among the various factors controlling the amyloid aggregation process, the influences of ions on the aggregation rate and the resulting structures are important aspects to consider, which can be studied by molecular simulations. There is a wide variety of protein force fields and ion models, raising the question of which model to use in such studies. To address this question, we perform molecular dynamics simulations of Aβ_{16-22}, a fragment of the Alzheimer's amyloid β peptide, using different protein force fields, AMBER99SB-disp (A99-d) and CHARMM36m (C36m), and different ion parameters. The influences of NaCl and CaCl$_2$ at various concentrations are studied and compared with the systems without the addition of ions. Our results indicate a sensitivity of the peptide-ion interactions to the different ion models. In particular, we observe a strong binding of Ca^{2+} to residue E22 with C36m and also with the Åqvist ion model used together with A99-d, which slightly affects the monomeric Aβ_{16-22} structures and the aggregation rate, but significantly affects the oligomer structures formed in the aggregation simulations. For example, at high Ca^{2+} concentrations, there was a switch from an antiparallel to a parallel β-sheet. Such ionic influences are of biological relevance because local ion concentrations can change in vivo and could help explain the polymorphism of amyloid fibrils.

KEYWORDS
Alzheimer's disease, amyloid aggregation, amyloid-beta, force fields, ion parameters, MD simulations

1 | INTRODUCTION

The role of the amyloid β peptide (Aβ) in the development of Alzheimer's disease (AD) has been the focus of research since the 1990s and is a central component of the amyloid cascade hypothesis.[1–3] It proposes that the accumulation of excess Aβ leads to neuronal loss and ultimately dementia. However, this is an oversimplification, especially when one considers that many aspects of AD pathogenesis that are downstream in the cascade, such as oxidative stress and inflammation, are also involved. A growing body of evidence suggests that there are a variety of positive feedback loops in AD,[4] where processes downstream in the cascade can stimulate processes upstream, and thus are likely to accelerate and increase the severity of AD, rather than a linear cascade. The fact that Aβ is prone to interact with other components in the brain complicates the aggregation pathway and poses serious challenges for therapeutic development. One of these types of interactions is with ions. Aβ is a negatively charged peptide under physiological conditions.[5] It is therefore expected to interact strongly with the most abundant ions like sodium (Na$^+$) and calcium ions (Ca^{2+}), which are known to play a role in neuronal function.[6,7] For example, impaired glutamate clearance and decreased levels of Na$^+$/K$^+$-ATPase in the brain have been reported to be associated

with AD, thereby disrupting the balance of monovalent alkali metal ions across neuronal membranes, which may significantly affect the electrophysiological activity of brain cells. In addition, the Ca^{2+} concentration around Aβ deposits was shown to be significantly increased in AD brains compared with physiological conditions, suggesting a role in AD development.[8,9]

Most studies evaluating the effects of metal ions on Aβ have been performed in vitro, but molecular dynamics (MD) simulation studies have also been performed for this purpose.[10] Instead of studying the full-length Aβ peptide, which requires considerable amounts of simulations and also wallclock time to obtain convergent MD trajectories for this intrinsically disordered protein (IDP),[11] one often resorts to studying smaller peptides, such as the Aβ_{16-22} peptide. Aβ_{16-22} is ideal for simulation studies because it requires less computational effort while aggregating into amyloid fibrils with antiparallel β-sheet orientation.[12] This peptide is also often used for benchmarking protein force fields and simulation methods, which was done for Aβ_{16-22} monomers,[13,14] dimers,[14–16] trimers,[17] and hexamers.[18,19] In our recent work, we have assessed the performance of different IDP force fields to reproduce the Aβ_{16-22} aggregation process up to hexamers,[13,18] and found them to be superior compared with the non-IDP force fields, as they also perform better in the modeling of the conformational ensemble of full-length Aβ and other IDPs.[16,20] In our investigation of Aβ, we conducted a thorough comparison between ensemble-averaged nuclear magnetic resonance (NMR) observables calculated from our simulations and corresponding experimental data.[20] We also assessed the correlation of the simulation data with structural and kinetic information that was determined by fluorescence spectroscopy. Our analysis revealed that only the CHARMM and AMBER force fields adapted for IDPs were capable of faithfully reproducing the diverse experimental values. To evaluate the performance of these IDP-adapted force fields in modeling amyloid aggregation, we devised two distinct approaches.[18,19] First, we examined their ability to replicate the experimental ranking of aggregation speed, spanning from no aggregation to rapid aggregation, as observed for different Aβ_{16-22} variants.[21] Additionally, we tested their capacity to model the ultimate aggregation end product, namely the Aβ_{16-22} amyloid fibril for which a solid-state NMR structure is available.[12] In both assessments, the IDP force field from the CHARMM family consistently outperformed those from the AMBER family, although the latter still demonstrated superior performance when compared with non-IDP force fields. What has not yet been addressed in these benchmark studies are the possible effects of ion concentration and also ion parameters on Aβ_{16-22} aggregation, which are, therefore, the focus of this study.

When it comes to choosing among the available ion parameters, one finds oneself in a zoo of possibilities. Apart from the fact that each of the large force fields from the CHARMM and AMBER families has its own ion parameters, there are many independently developed ion parameters that are suitable for different applications and differ in terms of the targeted experimental values.[22] The AMBER force fields use AMBER-adapted Åqvist parameters[23] for the cations and Dang parameters[24] for the chloride ion together with the SPC/E water model, which were developed to reproduce the experimental solvation free energies. Although it is known that these parameters lack a balance between ion-

water and ion-ion interactions and thus give rise to spontaneous crystallization,[25] these parameters are still widely used for the divalent cations, regardless of the chosen water model. Joung and Cheatham attempted to overcome most of the shortcomings of the Åqvist/Dang ion parameters for the monovalent alkali cations used with the SPC/E, TIP3P, or TIP4P EW water model by adding lattice energies and interionic distances.[26,27] As a result, the Joung-Cheatham ion parameters are now the default monovalent ion parameters for the AMBER force fields.[22] As for CHARMM, the initial ion parameters for Na^+ and K^+ were developed by Beglov and Roux,[28] and are still part of the official CHARMM36m (called C36m henceforth) distribution,[29] one of the force fields used here. Currently, the only anion available within C36m is chloride. Within the framework of fixed-charge nonpolarizable force fields, there is an increasing interest in scaled-charge schemes.[30] This approach allows us to include the effects of polarization in a mean-field way, that is, without introducing explicit terms for polarizability, by simply scaling the point charges of the ions.[31–35] This leads to ionic point charges which are no longer integers. For example, in the recently developed Madrid ion parameters, Na^+, Ca^{2+}, and Cl^- have charges of $+0.85$, $+1.70$, and $-0.85\ e^-$, respectively.[36,37] It is worth noting that the Madrid ion parameters were developed using the TIP4P-EW water model without a specific biomolecular force field in mind.

In this study, we compare of the effects of different ion concentrations and parameters on the structure and aggregation of Aβ_{16-22}. We test both NaCl and CaCl$_2$ at concentrations of 50 mM and 500 mM, and also include the case of no ions being added. Two all-atom force fields developed for IDPs, namely, AMBER99SB-disp (A99-d)[20] and C36m[29] are used. For the latter, we also test the implementation with enhanced protein-water interactions,[29] which we call here C36mW. For the ion parameters we consider the Åqvist, Joung-Cheatham, and Madrid parameters together with A99-d, and the default ion types for the C36m simulations. Using this set of force field/ion paramter combinations, we aim to identify the different influences of the protein force field, extra scaling of protein-water interactions (as possible via C36m), and ion parameters on the behavior of Aβ_{16-22}. We report results for monomeric and hexameric Aβ_{16-22} systems that we have studied using all-atom MD simulations on the µs time scale.

2 | METHODOLOGY

2.1 | Simulation details

We obtained the initial Aβ_{16-22} structure (shown in Figure 1) used for all systems as described in our previous publication.[13] The protonation states of the lysine and glutamic acid were assigned to correspond to pH 7.0 and were thus modeled as protonated and deprotonated, respectively. The N- and C-termini were capped using acetyl (ACE) and N-methylamide (NME) groups, respectively. We added no salts or either NaCl and CaCl$_2$ at concentrations of 50 or 500 mM. We considered three protein force fields, namely A99-d,[20] C36m,[29] and C36mW.[29] The latter is based on C36m but includes more favorable van der Waals interactions between protein and water. For A99-d, we used three different ion parameters: Åqvist[23] for the cations and

FIGURE 1 The starting structure of $A\beta_{16-22}$ used in all simulations.
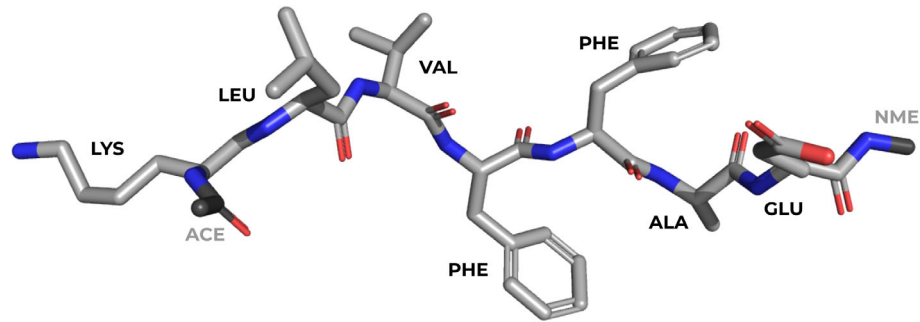
Dang[24] for the chloride, Joung-Cheatham,[26,27] and Madrid.[37] For C36m and C36mW, we employed the standard C36m ion parameters.

After solvation and addition of ions, we minimized the energy of each initial system using the steepest descent algorithm for 50 000 steps. For equilibration, we first performed constant-volume simulations at 300 K for 100 ps, followed up by constant-pressure simulations at 1 bar for another 100 ps. We obtained the production runs at 300 K and 1 bar using a 2 fs time step. During the equilibration simulations, we used, if applicable, the Berendsen barostat[38] and the Berendsen thermostat with velocity rescaling[39] using 2.0 and 0.1 ps time constants, respectively. For the production runs, we switched the barostat to the Parrinello-Rahman barostat[40] to keep the pressure at 1 bar with a time step of 2 ps. In all simulations, we constrained the length of all bonds using the LINCS algorithm[41] and kept the water molecules rigid using the SETTLE algorithm.[42] We applied the particle mesh Ewald (PME) method[43] to treat the electrostatic interactions with a real-space cutoff of 1.2 nm. For the van der Waals interactions, we used the force-switch algorithm between the distance range 1.0–1.2 nm. For the production runs, we simulated three independent runs, all continuing from the last step of the constant-pressure equilibration simulations. The monomer simulations were run for 2 μs each, while each hexamer simulation was 1 μs long. The total accumulated simulation time for this work is thus 153 μs. Further details of the simulation setup can be found in Table 1. All

TABLE 1 Details of the simulated systems.

Monomer simulations					
FF	Ion concentration (mM)	# of atoms	Box size (nm³)	# of ions	# water molecules
A99-d	0	15 330	4,9 × 4,9 × 4,9		3799
	50	15 336	4,9 × 4,9 × 4,9	3 Na, 3 Cl	3799
		15 327		3 Ca, 6 Cl	3796
	500	15 144	4,9 × 4,9 × 4,9	35 Na, 35 Cl	3735
		14 759		35 Ca, 70 Cl	3630
c36m/W	0	11 348	4,8 × 4,8 × 4,8		3738
	50	11 354	4,8 × 4,8 × 4,8	3 Na, 3 Cl	3738
		11 330		3 Ca, 6 Cl	3729
	500	11 226	4,8 × 4,8 × 4,8	35 Na, 35 Cl	3674
		11 144		34 Ca, 68 Cl	3636
Hexamer simulations					
FF	Ion concentration (mM)	# of atoms	Box size (nm³)	# of ions	# water molecules
A99-d	0	132 896	10 × 10 × 10		33 023
	50	132 956	10 × 10 × 10	30 Na, 30 Cl	33 023
		132 866		30 Ca, 60 Cl	32 993
	500	131 312	10 × 10 × 10	304 Na, 304 Cl	32 475
		130 400		304 Ca, 608 Cl	32 171
c36m/W	0	98 769	9,9 × 9,9 × 9,9		32 655
	50	98 829	9,9 × 9,9 × 9,9	30 Na, 30 Cl	32 655
		98 769		30 Ca, 60 Cl	32 625
	500	97 733	9,9 × 9,9 × 9,9	304 Na, 304 Cl	32 107
		97 125		304 Ca, 608 Cl	31 803

simulations were realized with the MD simulation software GRO-MACS version 2020.6.[44–47]

2.2 | Trajectory analysis

We performed the trajectory analysis using a combination of GRO-MACS 202X tools, the MDTraj Python library,[48] in-house Python scripts,[19] and ATRANET[49] for transition network calculation (https://github.com/strodel-group/ATRANET).

2.2.1 | Structural analysis

We computed the number of structural clusters for the $A\beta_{16-22}$ monomers using the *gmx cluster* command, which applies a nearest neighbor clustering algorithm based on the root mean square deviation (RMSD) between the structures[50] The RMSD was calculated between the backbone atoms of any two structures collected in a trajectory, and an RMSD cutoff of 0.2 nm was used to define neighborhood. We calculated the three-bond $^3J_{HN/HA}$ and two-bond $^2J_{N/CA}$ dipolar nuclear magnetic resonance (NMR) couplings using the equation $J = A\cos^2\theta + B\cos\theta + C$, where θ is the backbone torsion angle ϕ for the ^3J coupling and ψ for the ^2J coupling. We used the values $A = 7.09$, $B = -1.42$, and $C = 1.55$ for the ^3J couplings[51] and $A = 7.6213$, $B = -1.3791$, and $C = -0.2067$ for the ^2J couplings.[52] We calculated both the protein-water and intraprotein hydrogen bonds (H-bonds) using the *gmx hbond* command, setting the cutoff values for the hydrogen donor-acceptor angles and distances to 30° and 0.35 nm, respectively. The protein-ion contacts were determined using a cutoff distance of 0.5 nm between the peptide $C\alpha$ atoms and the ions. For the intrapeptide contacts, we used a 0.5 nm cutoff between the peptide non-hydrogen atoms. We computed the radial distribution function, denoted as $\rho(r)$, for the protein-ion and ion-ion pairs after removing the translational and rotational degrees of freedom from the trajectories using the *gmx rdf* command with a 0.2 nm bin width. The secondary structure of $A\beta_{16-22}$ was determined based on the backbone ϕ/ψ angles: an amino acid is defined to adopt a β-strand conformation if its ϕ/ψ angles fall within the polygon with the vertices at $(-180°, 180°)$, $(-180°, 126°)$, $(-162°, 126°)$, $(-162°, 108°)$, $-144°, 108°)$, $(-144°, 90°)$, $(-50°, 90°)$, and $(-50°, 180°)$; an α-helical content if within the polygon $(-90°, 0°)$, $(-90°, -54°)$, $(-72°, -54°)$, $(-72°, -72°)$, $(-36°, -72°)$, $(-36°, -18°)$, $(-54°, -18°)$, and $(-54°, 0°)$. All other angle pairs are considered as random coil.[53]

2.2.2 | Transition networks

We computed transition networks for the hexamer simulations by categorizing the system according to its overall β-strand content and maximum oligomerization state,[18,19,54] which can range from 1 for monomers only to 6 for the hexameric state. The β-strand content was determined based on the torsion angles along peptides'

backbones (see above). The transition network calculations were all realized with ATRANET[49] and the resulting transition networks were visualized with Gephi.[55]

3 | RESULTS AND DISCUSSION

### 3.1 | Structural characteristics of $A\beta_{16-22}$ monomers

We begin our analysis by investigating the conformational ensemble of the $A\beta_{16-22}$ monomers. We performed an RMSD-based clustering of the $A\beta_{16-22}$ monomers and monitored the number of clusters formed within the trajectory as a function of simulation time. Figure 2 shows that for all systems the number of different clusters converges to its maximum values within ~1000 ns. This happens slightly faster for the C36mW force fields compared with the others, with A99-d/Åq. requiring the longest simulation time to achieve convergence of the number of structural clusters. Moreover, for A99-d/Åq, the final number of clusters is the same regardless of the ion type and concentration. The largest number of clusters (above 20) is obtained for A99-d/JC at 500 mM NaCl, A99-d/Madrid at 500 mM $CaCl_2$, C36m without salt, and C36mW at 500 mM NaCl. However, the differences between the C36m and C36mW clustering results are minor and of almost no statistical significance, regardless of the ion type and concentration.

Next, we investigate the structures formed by the $A\beta_{16-22}$ monomers using the ^3J and ^2J-couplings to this end (Figure 3). These values could in principle be determined by NMR experiments, but such values have not yet been published. Therefore, we cannot correlate our simulation results with experiments. C36m and C36mW yield very similar ^3J and ^2J-coupling values. For the A99-d models, A99-d/JC and A99-d/Madrid are the most responsive to the presence of different types and/or concentrations of ions, while no significant response is seen for A99-d/Åq. C36m and C36mW predict larger ^3J-coupling values compared with the A99-d models, with the most notable difference for the A21-E22 bond. As a general trend, C36m and C36mW predict smaller ^2J-coupling values than the A99-d models for all bonds.

To understand the differences seen for the NMR dipolar couplings, we determined the secondary structure of $A\beta_{16-22}$. Figure 4 shows that the $A\beta_{16-22}$ monomers predominantly adopt the β-strand structure for ~70%–75% of the time, while α-helices formed with about 10% probability, and random coil structures occurred with ~15%–20% frequencies. This result is consistent with the structures that result from clustering the trajectories. The topmost clusters in Figure 2 are all extended structures. Similar structures were also found for the subsequent clusters. Only in some of the simulations were other structural elements such as turns or helices observed in the second cluster, which are also shown in Figure 2. The A99-d family generally predicts a larger population of α-helical structures compared with C36m/C36mW. Within the A99-d family, increasing the ion concentration increases the α-helix formation independent of the
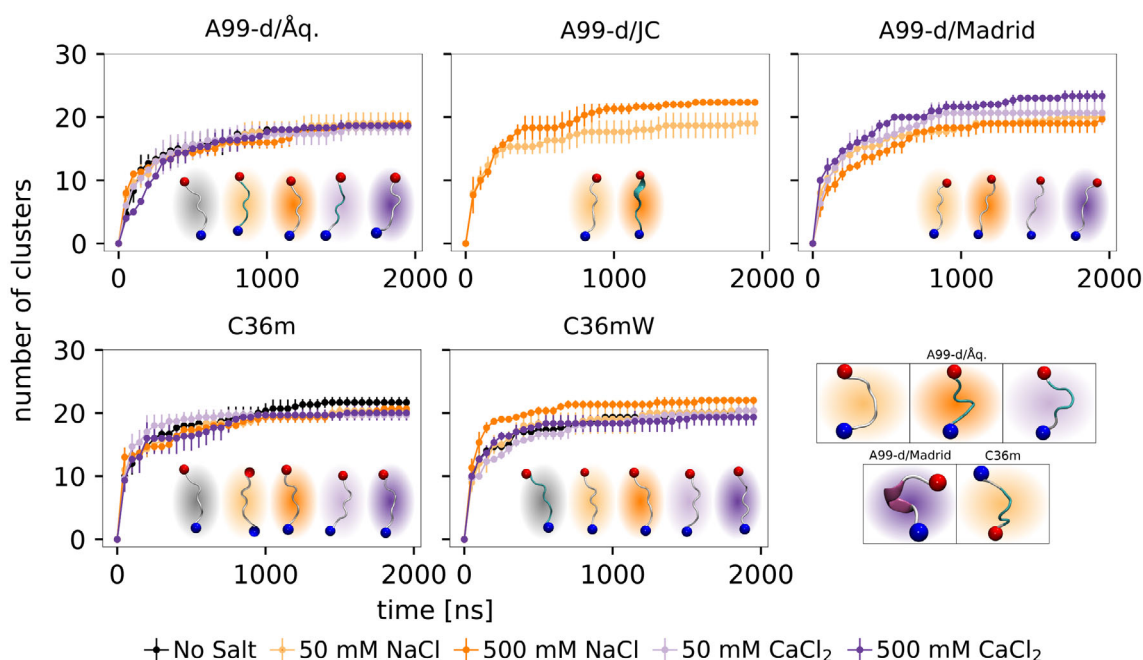
FIGURE 2 Number of structural clusters of monomeric $A\beta_{16-22}$ as a function of time for the different protein and ion models (see label above each panel) and salt types and concentrations (see color code at the bottom). The result without salt added (black) simulated with A99-d is only shown once in the top left panel. The values are reported as the mean and standard error of the mean over three independent trajectories per system. For each simulation, the $A\beta_{16-22}$ structure representing the top cluster of each simulation (indicated by the color cloud surrounding the peptide) is shown. For some of the simulations, also the representative structure of the second cluster is displayed (bottom right). $A\beta_{16-22}$ is shown as cartoon, with the N- and C-termini being indicated by blue and red spheres, respectively.
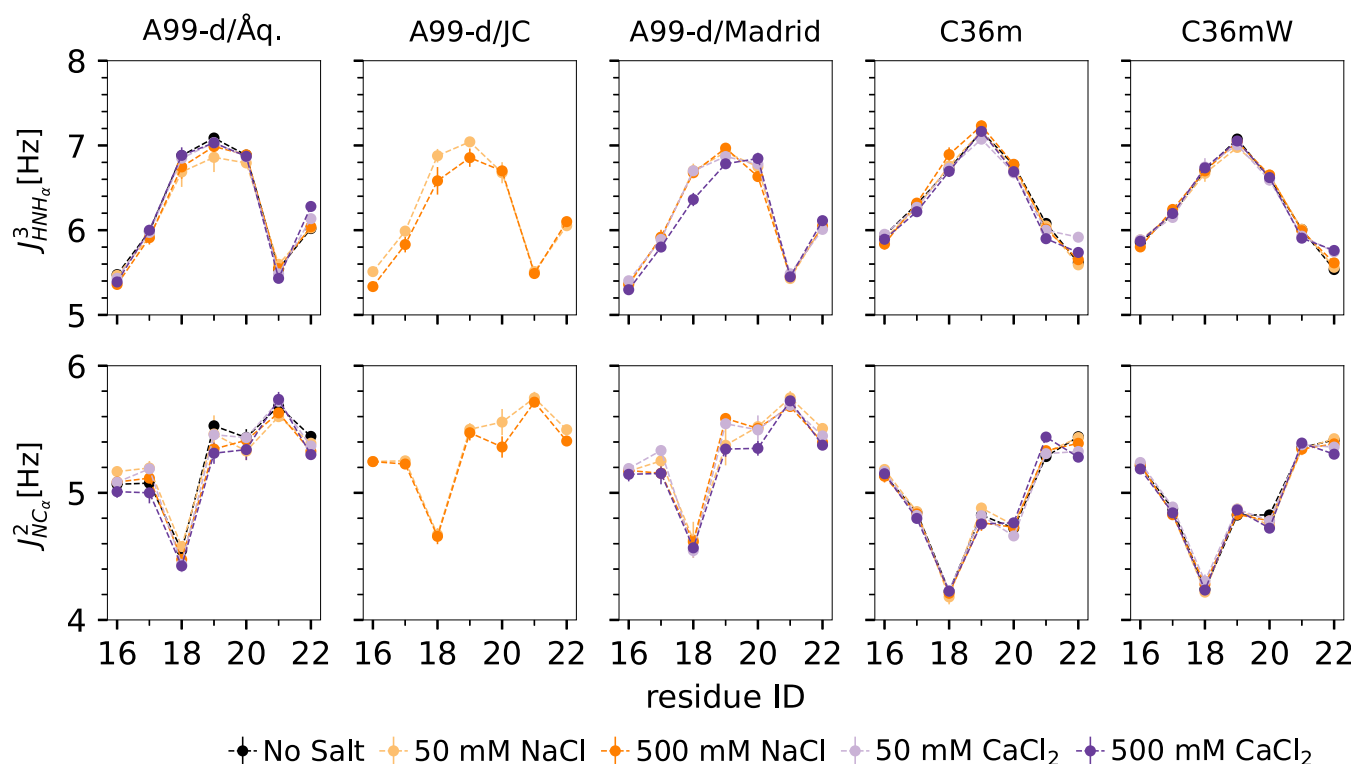
FIGURE 3 The three-bond $^3J_{HN/HA}$ (top) and two-bond $^2J_{N/CA}$ couplings (bottom) of monomeric $A\beta_{16-22}$ for the different protein and ion models (see labels on the top) and salt types and concentrations (see color code at the bottom). The results without salt added (black) simulated with A99-d are only shown once in the most left panels. The values are reported as the mean and standard error of the mean over three independent trajectories per system.
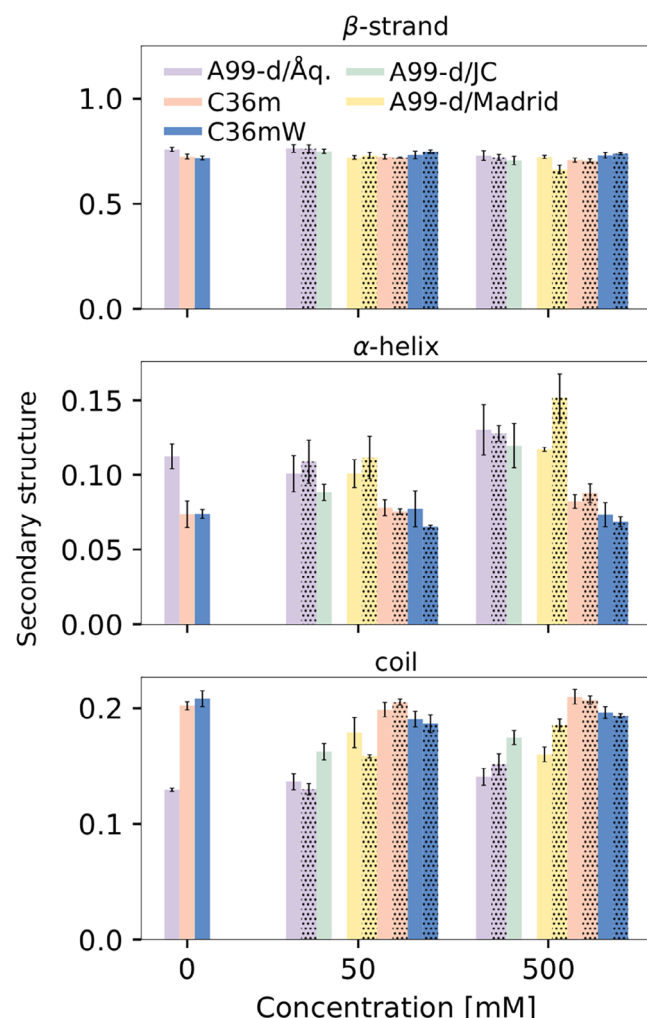
FIGURE 4 Population of the secondary structure elements β-strand (top), α-helix (middle), and random coil (bottom) in monomeric Aβ_{16-22} for the different salt concentrations (x-axis) and for the different force fields (see color code at the top). The dotted bars represent the systems with Ca^{2+}. The results for no salts added simulated with A99-d are shown as lilac (A99-d/Åq.) but also serve as a reference for A99-d/JC and A99-d/Madrid. The values are averaged over three independent trajectories per system, and the error bars correspond to the standard error of the mean.

ion model. Changing the cation from Na$^+$ to Ca^{2+} increases the α-helix population by about one third for A99-d/Madrid at 500 mM salt concentration. The C36m and C36mW predictions for the α-helix population are insensitive to the ion type and concentration. With regard to the random coil populations, both C36m and C36mW yield significantly larger random coil populations compared with the A99-d family for all ion types and concentrations, but in particular when no ions are present. Within the A99-d family, increasing the ion concentration increases the random coil population, with the largest response seen for the Madrid ion parameters and the smallest one for A99-d/Åq. Changing the cation from Na$^+$ to Ca^{2+} decreases the random coil population at 50 mM salt concentration for both A99-d/Åq. and A99-d/Madrid (for A99-d/JC there are no Ca^{2+} parameters), while the opposite takes place with 500 mM salt. Yet the changes are

greater for A99-d/Madrid than for A99-d/Åq. For A99-d/JC, the amount of random coil increases with increasing Na$^+$ concentration and is between the predictions by the other two ion models at 50 mM Na$^+$ and is the highest among the A99-d results at 500 mM Na$^+$, yet lower than for A99-d/Madrid at 500 mM Ca^{2+}.

3.2 | Aβ_{16-22}-ion interactions

Having examined the effects of ions on the secondary structure of Aβ_{16-22} monomers, we turn our attention to protein-ion contacts, since they are thought to be closely associated with structure formation. We computed the number of contacts between the cations and the non-hydrogen atoms of the peptide residues. The results in Figure 5 show large differences between the protein force fields and ion parameters. Na$^+$, in agreement with previous observations for Aβ_{16-22},[56,57] shows almost no binding to the Aβ_{16-22} peptide, except for C36mW at 500 mM NaCl. Ca^{2+} can bind to E22 as a result of electrostatic attraction, yet only in A99-d/Åq., C36m, and C36mW. The amount of bound Ca^{2+} is almost twice as large for C36m and C36mW compared with A99-d/Åq. Cl$^-$ shows slight binding to K16 but only at 500 mM concentration of either salt, except for the JC and Madrid ion parameters. C36m and C36mW have twice the number of bound Cl$^-$ compared with A99-d/Åq. It is interesting to note that for the C36m and C36mW force fields, we also observe possible Cl$^-$ binding at the negatively charged E22 when the CaCl$_2$ concentration is high. In this case, significant Ca^{2+} binding occurs at this site, which can also pull Cl$^-$ into the vicinity of E22.
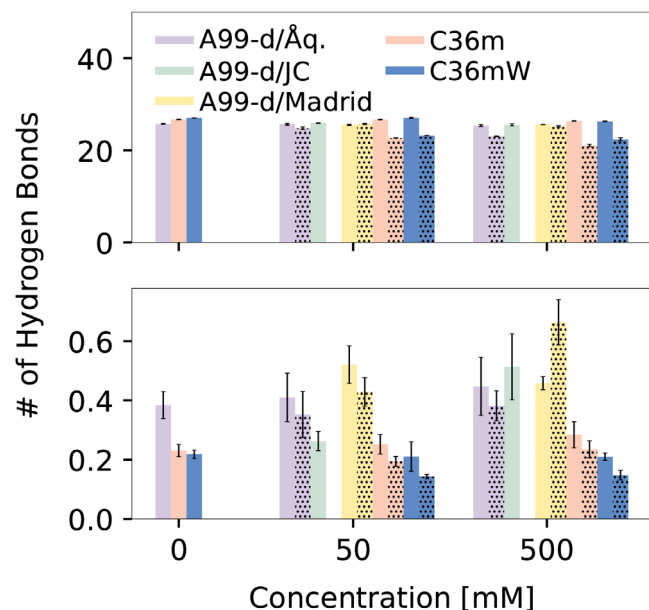
3.3 | Intrapeptide and peptide-water hydrogen bonding

We finalize our analysis of the Aβ_{16-22} monomers by calculating the number of intrapeptide and Aβ_{16-22}-water H-bonds. The results in Figure 6 show that C36m and C36mW predict significantly fewer intrapeptide H-bonds compared with the A99-d models, and the number decreases when we change the cation from Na$^+$ to Ca^{2+}. This correlates with our observations from the secondary structure analysis (Figure 4), in particular with the reduced helical content with C36m and C36mW that requires H-bonding between residues. The highest number of intrapeptide H-bonds is formed with the A99-d/Madrid model. Furthermore, when the ion concentration is increased to 500 mM and when the cation is changed from Na$^+$ to Ca^{2+}, A99-d/Madrid predicts a 50% increase in the number of intrapeptide H-bonds, whereas A99-d/Åq. is rather unresponsive. This also correlates with the secondary structure results and can be explained by a decrease in peptide-water interactions due to the presence of ions, which favors the formation of H-bonds within the peptide. The analysis of the peptide-water H-bonding confirms this conclusion. In general, A99-d, C36m, and C36mW yield similar values for the number of H-bonds formed between Aβ_{16-22} and water. Changing the cation from Na$^+$ to Ca^{2+} decreases the peptide-water H-bonding with C36m
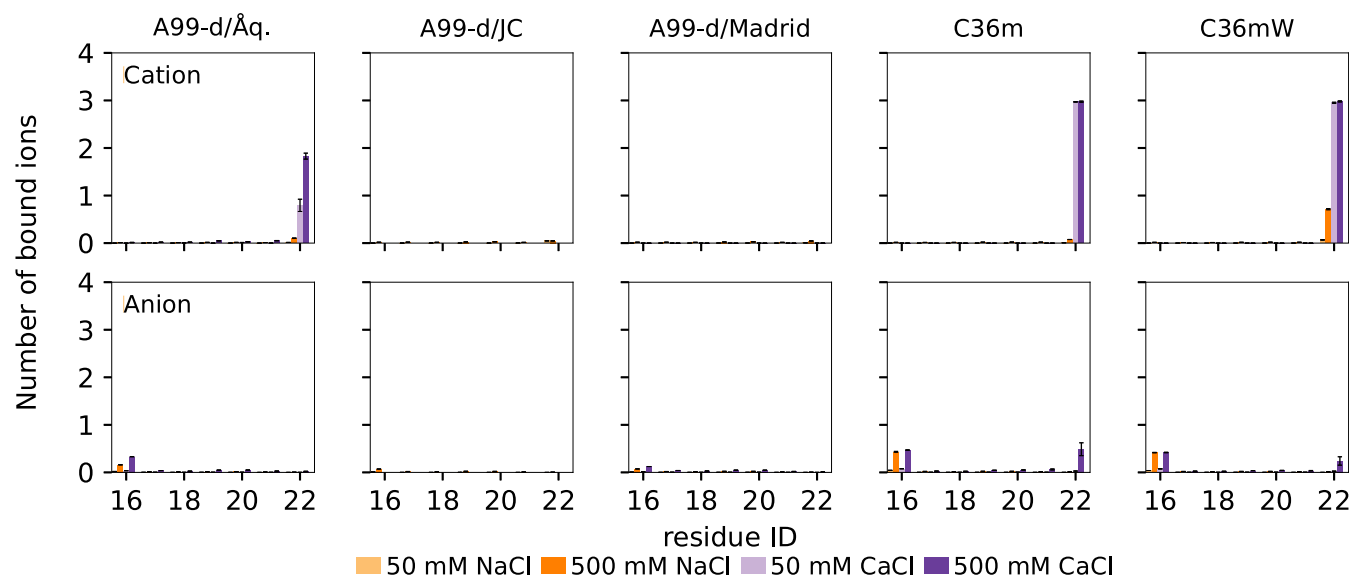
FIGURE 5 The average number of bound cations (top) and anions (bottom) to the $A\beta_{16-22}$ residues (x-axis) for the different force fields (see labels at the top) at various ion concentrations (see color code at the bottom). An ion is considered to be bound whenever it is within 0.5 nm of the Cα atom of a residue, explaining that more than one ion can be bound to a residue. The numbers of cations in these systems are 3 for all 50 mM NaCl and CaCl$_2$ systems, 34 for the C36m and C36mW systems at 500 mM CaCl$_2$, and 35 for the C36m and C36mW systems at 500 mM NaCl as well as for the A99-d systems at 500 mM salt. The values are averaged over three independent trajectories per system, and the error bars correspond to the standard error of the mean.

and C36mW at both 50 mM and 500 mM salt concentrations, which correlates with the tight binding of Ca^{2+} to E22 (Figure 5). For the A99-d models, a difference between ion types is observed only at a


FIGURE 6 The average number of H-bonds between monomeric $A\beta_{16-22}$ and water (top) and within the peptide (bottom) for the different force fields (see color code) and at various ion concentrations (x-axis). The dotted bars correspond to the systems with Ca^{2+}. The results for no salts added simulated with A99-d are shown as lilac (A99-d/Åq.) but also serve as a reference for A99-d/JC and A99-d/Madrid. The values are averaged over three independent trajectories per system, and the error bars correspond to the standard error of the mean.

concentration of 500 mM and only for A99-d/Åq, which also predicts a decrease in peptide-water H-bonding when switching from Na$^+$ to Ca^{2+} and is consistent with the ion binding affinity shown in Figure 5. The A99-d/Madrid model does not lead to a significant change in the number of protein-water H-bonds. This means that the response of the C36m force fields to the change in ion type is larger than that of the A99-d models.

3.4 | Interionic interactions

We now switch our perspective to the ion-ion interactions and present the cation–cation and cation-anion radial distributions (Figure 7). Overall, we see very large differences between the A99-d and C36m/C36mW force fields, which is clearly evident from the cation-anion $\rho(r)$ profiles. For all cation-anion pairs and at all concentrations, C36m and C36mW predict stronger interactions compared with the A99-d models. For Ca^{2+}-Cl$^-$, we see direct ion pairing with C36m/C36mW, indicated by a pronounced $\rho(r)$ peak at $r \sim 0.25$ nm, while this peak is mostly small to non-existent in the A99-d models. A first $\rho(r)$ peak much higher than the second indicates close contact between the cation and the anion as a result of direct ion pairing, while a first $\rho(r)$ peak of similar height or lower than the second indicates that water enters between the two ions, suggesting solvent-separated ion pairs (i.e., indirect ion pairing). With regard to $\rho(r)$ for Na$^+$-Cl$^-$, we also see direct ion binding in the C36m, C36mW, and A99-d/Åq. models. The degree of direct ion pairing generally increases with increasing ion concentration from 50 to 500 mM of NaCl and CaCl$_2$, but no permanent ion aggregation or even crystallization was observed in the
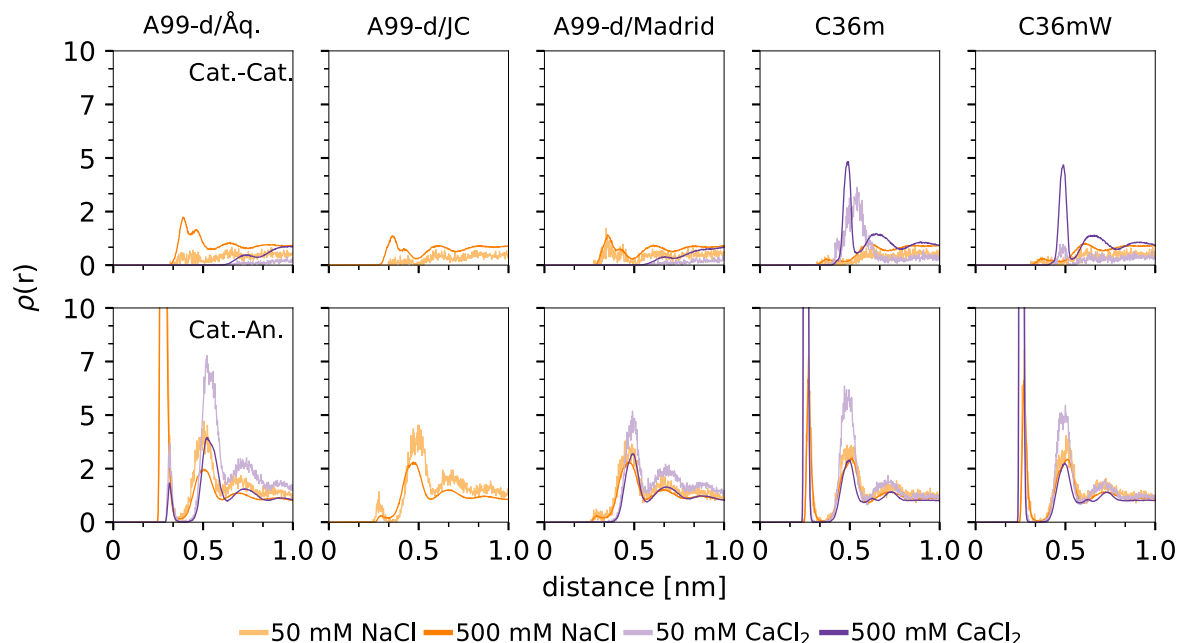
FIGURE 7 The radial distribution $\rho(r)$ for the cation–cation (top) and cation-anion (bottom) pairs for the different force fields (see labels at the top) and the different salt types and concentrations (see color code at the bottom).
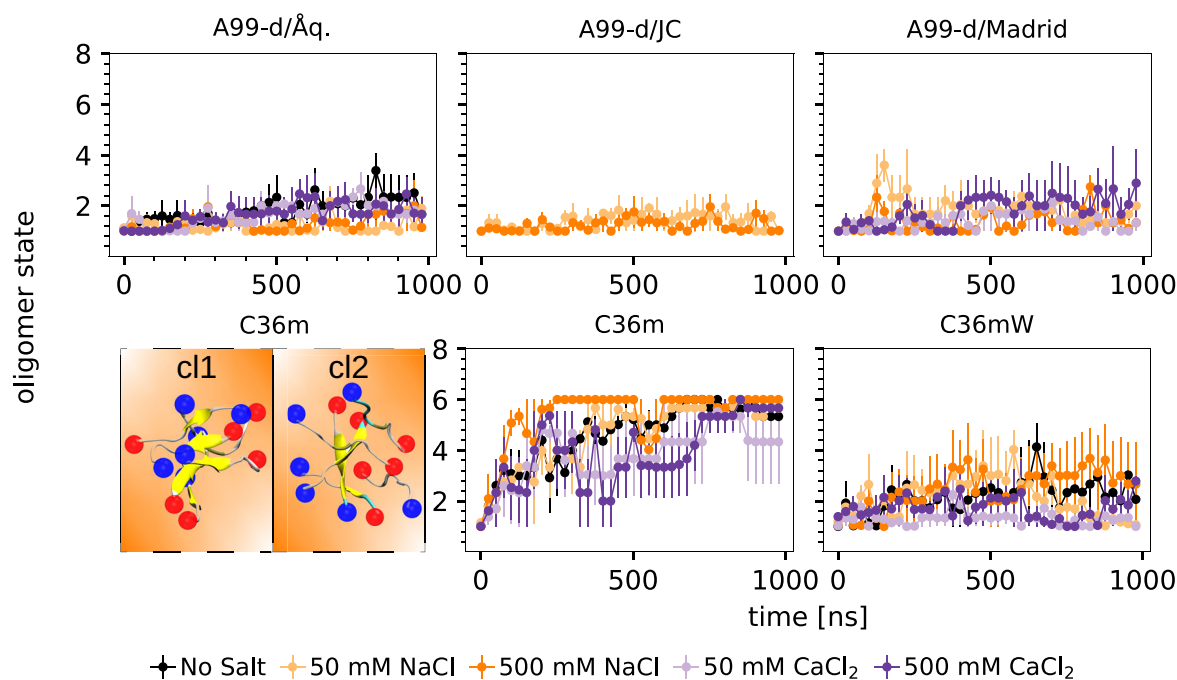
FIGURE 8 Average Aβ_{16-22} oligomer size as a function of time for the different force fields (see labels above each panel) and the different salt types and concentrations (see color code at the bottom). The result without salt added (black) simulated with A99-d is only shown once in the top left panel. The values are reported as the mean and standard error of the mean over three independent trajectories per system. In the lower-left corner, the two most populated hexamer structures are shown, resulting from clustering of the trajectories obtained with C36m at 500 mM NaCl. The peptides are shown as cartoons, with the yellow arrows indicating β-sheets.

simulations. The extent of indirect ion pairing is greater for Ca^{2+} than for Na$^+$, which can be explained by the higher charge density of Ca^{2+}, which causes electrostatic attraction of Cl$^-$ beyond the first and even second water shells surrounding this cation. The cation–cation radial

distributions show mostly low-intensity peaks due to electrostatic repulsion between them (Figure 7). Nevertheless, some peaks in $\rho(r)$ of considerable intensity are observed for Na$^+$-Na$^+$ in A99-d/Åq. and Ca^{2+}-Ca^{2+} in C36m and C36mW, especially at 500 mM salt

concentration. This surprising finding results from the attraction of these cations to E22, which allows two or more cations to approach each other (Figure 5).

3.5 | Oligomerization of Aβ_{16-22}

Next, we study the influences of ion concentration and parameters on the aggregation of Aβ_{16-22}. In each system, the six Aβ_{16-22} monomers were initially placed such that there were no peptide–peptide interactions in order not to bias the subsequent aggregation process. We consider the peptides to be assembled when the distance between any non-hydrogen atoms of two peptides or existing is less than 0.5 nm. We then calculated the maximum oligomer size as a function of simulation time to measure how fast the peptides aggregate. Figure 8 shows that C36m is the only force field that leads to aggregation to the hexameric state. Here, aggregation is fastest at 500 mM NaCl, followed by aggregation at 50 mM NaCl and without salt, which proceed at similar rates, while the presence of CaCl$_2$ seems to slow down the aggregation process. Thus, the binding of Ca^{2+} to E22 inhibits the aggregation as this reduces the electrostatic attraction between A16 and E22 that drives the initial aggregation.[16] Interestingly, Na$^+$ at high concentrations exerts the opposite effect. A possible explanation is that without the presence of any ions, the initial A16-E22 interaction is very tight, which slows down the reorientation into oligomers capable of growth. The growth-competent oligomers involve the formation of β-sheets, as the most populated hexamer structures in Figure 8 demonstrate.

A similar observation on the influence of NaCl on amyloid aggregation was made in a recent simulation study in which the aggregation of amphipathic peptides into amyloid-like fibrils was investigated under various internal and external conditions.[58] The internal conditions were altered by studying different sequences Ace-(XKXE)^2-NME, where X stood for F, L, V, or A, whereas the different external conditions included changes in temperature and NaCl concentration. For the peptides containing the less hydrophobic amino acids, particularly for X = A, NaCl was found to favor aggregation. One explanation for this is that for the more hydrophobic amino acids X aggregation is driven by hydrophobicity, so electrostatic interactions are less relevant, whereas for the less hydrophobic X hydrophobic interactions become more important when electrostatic interactions are screened. However, as noted above, this argument also implies that electrostatic interactions, which also play a role in promoting aggregation, are not the crucial factor for β-sheet formation, which is required for amyloid aggregation.

In terms of aggregation rate, C36m is followed by C36mW, albeit at a significant distance. Within 1 μs, C36mW does not yield stable hexamers. Similar to C36m, C36mW at 500 mM NaCl also leads to larger oligomers faster than under the other conditions, while little to no aggregation is observed in the presence of CaCl$_2$. For A99-d/Åq. and A99-d/Madrid, the opposite trend is obtained compared with C36m/C36mW: aggregation is slowest in the presence of NaCl and it is fastest without any ions and in the presence of 500 mM CaCl$_2$. In particular, when no ions were added, the largest average oligomer size (tetramers and pentamers for a short time) was detected. The largest

oligomer size decreased significantly as ions were added to the system, indicating their efficiency in screening charge–charge interactions that drive the initial aggregation process. For this, Ca^{2+} is more effective than the single-charged Na$^+$. However, it should be noted that with A99-d the aggregation is generally slower than with C36m and C36mW, which agrees with our previous findings.[13]

3.6 | Aggregation pathways

A more detailed understanding of the aggregation pathways is provided by transition networks as shown in Figure 9. Here, the nodes indicate the state of Aβ_{16-22} categorized by the oligomer size (vertical axis) and the β-sheet content (horizontal axis). The size of the nodes reflects the population of the different Aβ_{16-22} oligomer states, and the number of transitions between them is shown by (undirected) edges of different thickness. The transition networks reveal significant differences between the different protein and ion models. With C36m, the transition networks are dominated by the hexamers with high β-sheet content; no hexamers with less than 40% β-sheet content are observed. Here, the presence of 500 mM salt, particularly CaCl$_2$, caused a slight reduction in β-sheet formation. In terms of formation of Aβ_{16-22} hexamers, C36m is followed by the C36mW force field. The A99-d models yielded the lowest population of the Aβ_{16-22} hexamers. All A99-d/ion combination as well as C36mW led to a high population of Aβ_{16-22} monomers with large β-strand content, which are stabilized by the increased peptide-water dispersion interactions in these models. This suggests that these monomers could aggregate to oligomers with a high content of β-sheets, since no internal conformational changes would be required, but the kinetics of aggregation is very slow. Increasing the NaCl concentration increases the aggregation in C36mW (and also C36m). It can be assumed that the presence of the ions replaces some of the peptide-water interactions, weakening the influence of the water model on the peptide's behavior. As already explained above, the same argument does not apply to Ca^{2+}. With A99-d, the amount of β-sheet is also generally high and in combination with the Åq. and JC ion parameters, monomers are the preferred species. Only for the Madrid ion parameters, the picture slightly changes in favor of dimers and trimers at 50 mM NaCl, which as interesting as with these ion parameters the least Aβ_{16-22}-ion interactions were observed. Thus, the interplay between peptide, water and ions is affected by more than direct interactions that were measured here. For both the force field and the ion model and type, we can see that increasing the salt concentration leads to a larger number of oligomeric states and more interconnectivity in the transition networks.

## 3.7 | Interprotein contacts in Aβ_{16-22} oligomers

We finalize our analysis by discussing the interpeptide residue-residue contacts. As before, a contact is defined when the distance between any two non-hydrogen atoms from residues of different Aβ_{16-22}
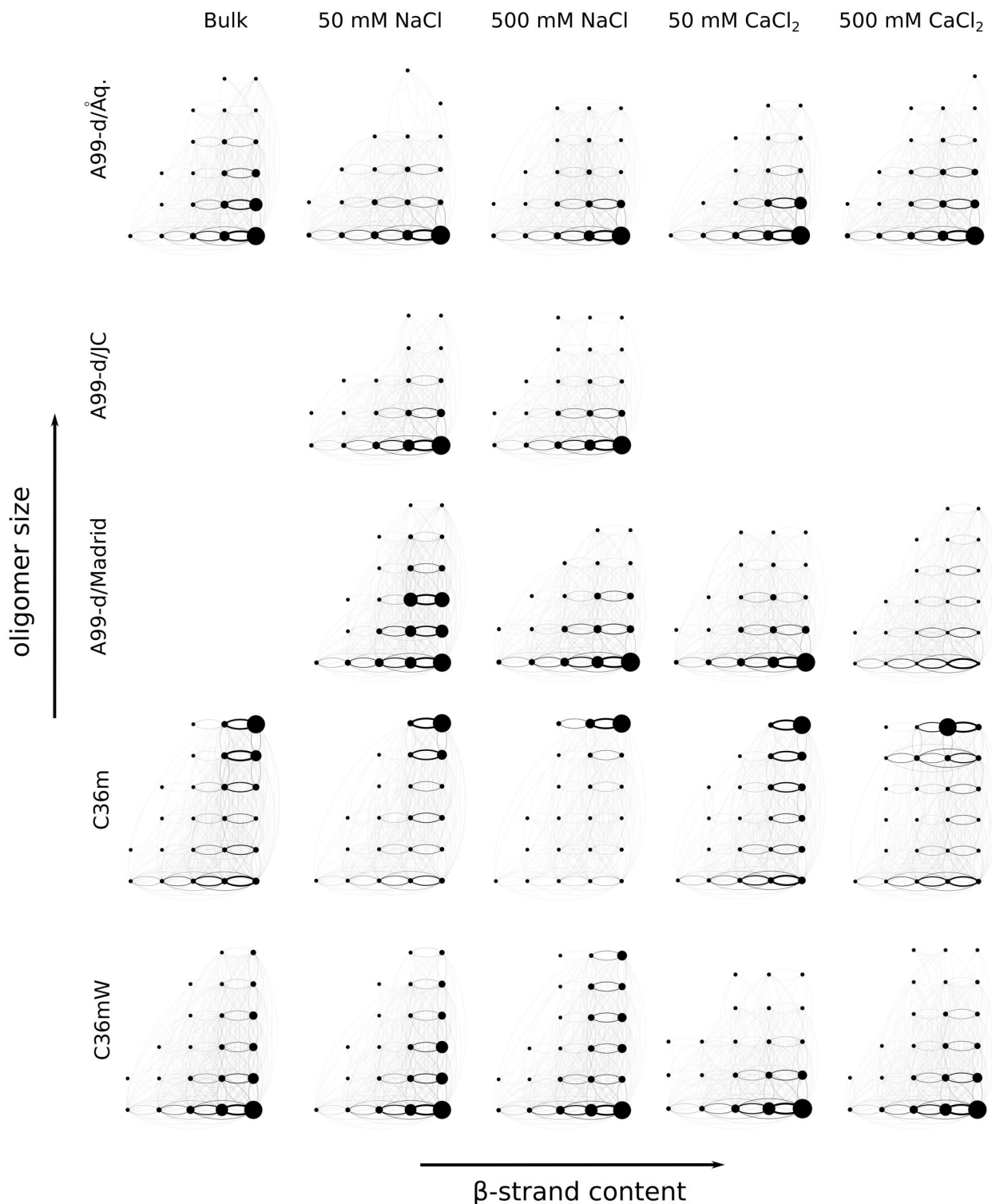
FIGURE 9 Transition networks for the aggregation of Aβ_{16-22} under different salt conditions (see labels at the top) for different force fields (see labels on the left). The oligomer size (from monomer to hexamer) is given along the vertical axis and the horizontal axis represents the β-strand content (divided into five ranges: 0%–20%, 20%–40%, etc.). The size of the nodes is proportional to the population of the state, and the width of the edges is proportional to the mass flux between the states. For calculating the transition networks, we concatenated three 1 μs trajectories per system. The results without salt (denoted as "bulk") obtained with A99-d are only shown once (for A99-d/Åq. in the top row) but also serve as a reference for A99-d/JC and A99-d/Madrid.

peptides falls below 0.5 nm. The results in Figure 10 show that different force fields give rise to considerably different interpeptide

contacts. In general, C36m and C36mW yielded more pronounced contacts connected with ordered oligomer structures than the A99-d
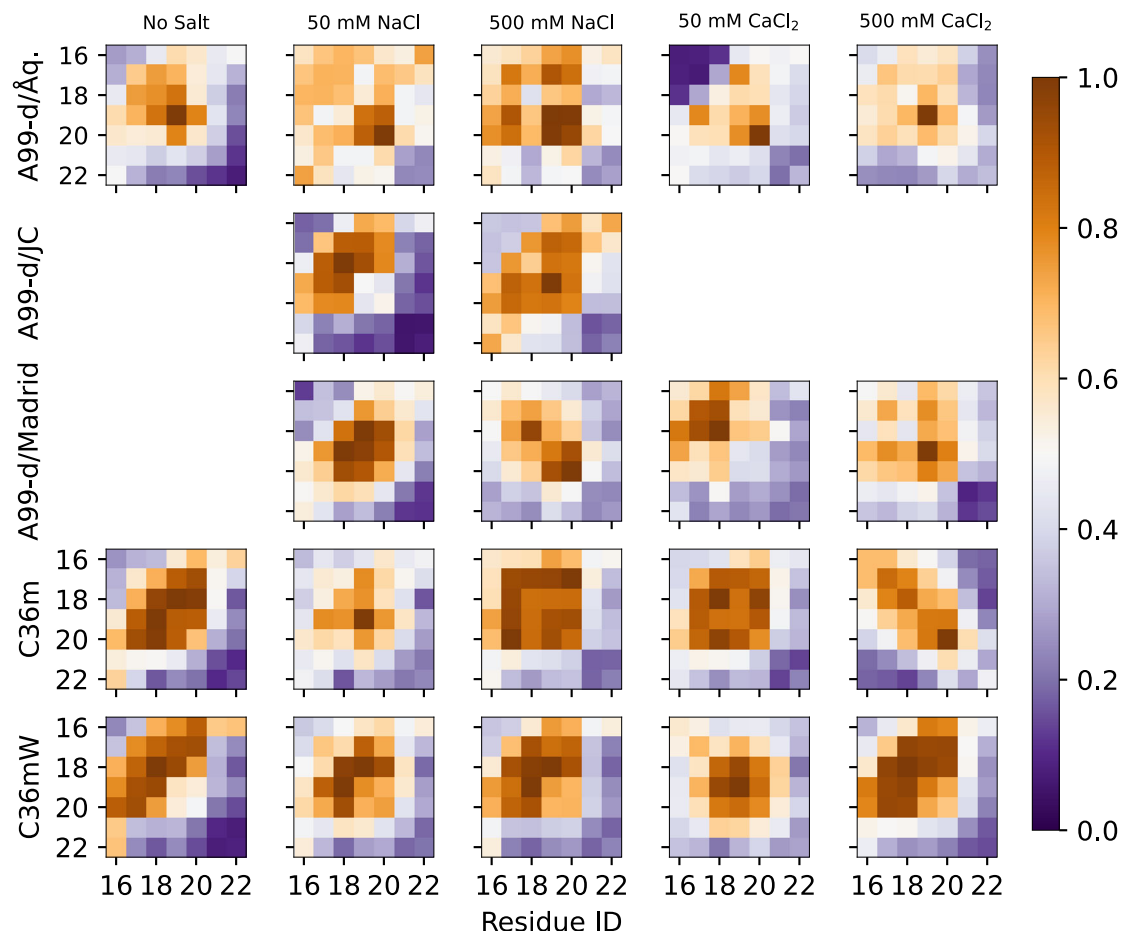
FIGURE 10 Probability of residue-residue contacts (see the color scale on the right) between $A\beta_{16-22}$ peptides in oligomers under different salt conditions (see labels at the top) for different force fields (see labels on the left). The results without salt (denoted as "bulk") obtained with A99-d are only shown once (for A99-d/Åq. in the top row) but also serve as a reference for A99-d/JC and A99-d/Madrid. The results are averages over the three simulations per system.

models. Without salt, both C36m and C36mW led to antiparallel alignments of the peptides with K16-E22 contacts due to salt bridge formation between them, which stabilizes this orientation in $A\beta_{16-22}$ aggregates.[12] With A99-d without salt, a tendency for parallel alignment is observed instead, yet without K16-K16 or E22-E22 contacts. Thus, the termini point away in this arrangement and the parallel alignment is driven by hydrophobic interactions spanning the L17-F20 region, with a dominant F19–F19 interaction.

The inclusion of salt leads to less ordered aggregates in many cases, as now the ordering electrostatic interactions between the termini are screened. This applies to C36m, C36mW, and the A99-d models. Exceptions are the aggregates formed at 500 mM $CaCl_2$ modeled with either C36m or C36mW. For C36m, a clear signature of parallel β_{16-22}-sheets emerged, that even includes K16-K16 contacts but no E22-E22 contacts. Here, E22 was found to be bound to Ca^{2+}, which explains that the parallel alignment became possible, with F20-F20 as the most dominant contact. Therefore, the different aggregation kinetics seen for C36m at 500 mM compared with the other C36m conditions may also be associated with the formation of a different aggregate morphology. With C36mW, the antiparallel alignment between the peptides remains the major interaction

pattern, yet to different degrees and a shift by two to three residues in the antiparallel alignment emerged. This is best seen for C36m at 500 mM $CaCl_2$, where, for instance, K16 of one peptide interacts not with E22 of the other peptide, but with F19 and F20; L17 interacts with V17-F20 and so on. For the A99-d models, it is difficult to identify specific interaction patterns upon the inclusion of ions. Some exceptions are A99-d/JC where off-register antiparallel β-sheets formed. For A99-d/Madrid, a tendency for antiparallel alignment is seen at 50 mM NaCl and 50 mM $CaCl_2$, which turned into a parallel alignment at 500 mM NaCl and no alignment at all at 500 mM $CaCl_2$. With A99-d/Åq., there is also no preferred alignment visible. Common to almost all interaction patterns obtained with A99-d is the high preference for interactions between two phenylalanine residues, which must therefore be specific to this force field.

4 | CONCLUSIONS

In this work, we simulated $A\beta_{16-22}$ as a monomer and as a system containing six copies of this peptide in the absence and presence of salt, either NaCl or $CaCl_2$, at different concentrations (50 and

500 mM) using different protein and ion models to investigate the effects of ions on the structure and aggregation of $A\beta_{16-22}$. The structural results of the $A\beta_{16-22}$ monomer simulations showed small differences depending on the ion type, concentration, or model, which may seem unimportant but proved relevant to the subsequent aggregation. The structural differences were evident in the NMR dipolar couplings and secondary structure of monomeric $A\beta_{16-22}$, and they could be partly linked to the peptide-ion interactions that are of different strength in the different models. The most significant structural difference is that C36m and C36mW predict a lower α-helical propensity for $A\beta_{16-22}$ than the A99-d models, which correlates with a smaller number of intraprotein H-bonds that formed with C36m and C36mW. These differences are due in part to the protein force fields, but also in part to the different behavior of the ion models tested. The Ca^{2+} ion binds with a high probability to E22 in the simulations with C36m and C36mW, but also with A99-d/Åq., while it does not bind with the A99-d/Madrid model. This observation correlates with an increase in α-helix upon a change from Na^+ to Ca^{2+}, especially at a salt concentration of 500 mM, in the case of A99-d/Madrid, while E22-Ca^{2+} interactions seem to counteract helix formation in $A\beta_{16-22}$. The different behavior of Ca^{2+} is also evident in the interionic interactions determined by radial distribution functions. In C36m and C36mW, this ion is much more involved in cation-anion and cation–cation interactions than in the A99-d models or is the case for Na^+.

With respect to $A\beta_{16-22}$ aggregation, we find that three effects have a relevant impact on the aggregation kinetics and the resulting aggregate structures. The kinetics is mainly determined by the peptide-water interactions, with an increase in the van der Waals interactions between the peptide and water decreasing the rate of aggregation. This leads to the slowest aggregation with A99-d and the fastest aggregation with C36m, and C36mW lies between these two extremes. Small variations in the aggregation speed were caused by the presence of NaCl and $CaCl_2$ at different concentrations, in particular by Ca^{2+}, but depending on the $A\beta_{16-22}$-Ca^{2+} binding intensity, different effects were observed. With C36m, C36mW, and A99-d/Åq., the aggregation rate is reduced at 500 mM $CaCl_2$, as here, the initial electrostatic attraction between K16 and E22 from different $A\beta_{16-22}$ peptides is screened due to Ca^{2+} binding to E22. With A99-d/Madrid, where no Ca^{2+} binding to the peptide was observed, the aggregation rate is increased, probably by weakening the peptide-water interactions due to the presence of large amounts of ions.

The ions also affect the aggregate morphology, for the same reasons as the aggregation kinetics is modified. For example, the orientation in the β-sheets changed from antiparallel to parallel when moving from a condition with no added salt to 500 mM $CaCl_2$ with C36m, or the antiparallel orientation shifted by two or three residues, as was the case for C36mW in the presence of NaCl (50 and 500 mM) and 500 mM $CaCl_2$ with respect to the corresponding salt-free simulation. In the simulations with A99-d, the addition of salt also caused changes in the resulting aggregate structures. However, the oligomers are less ordered than those obtained with C36m and C36mW. This is due to the slightly stronger preference for helical $A\beta_{16-22}$ structures observed in the monomer simulations with A99-d, as well as a higher

driving force for aggregation caused by hydrophobic interactions (in particular F-F assembly) compared with the C36m(W) modeling. In general, it can be observed that electrostatic interactions play a more important role in C36m(W) than in the A99-d models, which is evident from the peptide-ion, ion-ion, and peptide–peptide interactions.

In summary, our results show that not only the choice of protein force field and water model affect the results of amyloid aggregation simulations, but also the choice of ion parameters as well as ion concentration. However, it is fair to say that the effects of the former are greater than those of the latter. Which of the force fields and ion models creates the most realistic results for $A\beta_{16-22}$ is difficult to judge due to the missing experimental data for $A\beta_{16-22}$ monomers. On the other hand, for A99-d we have previously shown that this force field does not support modeling of the end product of amyloid aggregation, that is, amyloid fibrils.[13] In the simulations of a minifibril involving two β-sheet layers with six peptides forming an in-register, antiparallel βsheet in each layer, the A99-d force field led to the dissolution of the minifibril within 300 ns, while with C36m and C36mW this arrangement remained stable. This agrees with the very slow aggregation speed found here with A99-d.

The observation that the salt type and concentration impact the aggregation rate and the resulting structures is of high biological relevance. This is supported by a recent study by Yamazaki et al.[59] of $A\beta_{16-22}$ aggregation using both experiments and MD simulations. They demonstrated that the fibrillation kinetics follows the nucleation-elongation model, in which the aggregation nucleus consists of 6–7 peptide molecules that form two β-sheets that connect via their hydrophobic surfaces (as also seen here in the hexamers). In addition, also consistent with our findings, their experimental results showed that the addition of small amounts of salt or organic solvent has a significant effect on the fibril morphology, suggesting that electrostatic and hydrophobic interactions are important for fibril formation and structure selection. In a recent study, we have shown that the presence of strongly negatively charged glycosaminoglycans can lead to a depletion of cations in their vicinity as they are in close proximity to the glycosaminoglycans.[60] This had a major impact on the $A\beta$ structure present in the same simulation, which underwent a transition from disordered to ordered structures due to intrapeptide electrostatic deshielding by the abstraction of Na^+, causing the formation of β-sheet structures. Experimentally, glycosaminoglycans were observed to promote amyloid aggregation,[61] which might also be related to the local changes in salt concentration by the glycosaminoglycans, as we have shown here for the aggregation rate of $A\beta_{16-22}$ by simply changing the salt concentration in the simulation system. Finally, the finding that changes in aggregate structure can be caused by changes in ion type and ion concentration is also important with respect to the polymorphism of amyloid fibrils, which is a remarkable but still largely unexplained feature of amyloids.[62,63]

AUTHOR CONTRIBUTIONS

Eva Smorodina: Investigation; data curation; visualization; writing – original draft; formal analysis. **Batuhan Kav:** Investigation; conceptualization; methodology; writing – original draft; supervision; formal

analysis; visualization; validation; software. **Hebah Fatafta:** Writing – original draft; writing – review and editing; visualization; validation; formal analysis. **Birgit Strodel:** Conceptualization; methodology; validation; writing – review and editing; funding acquisition; supervision; resources; project administration.

CONFLICT OF INTEREST STATEMENT

The authors declare that the research was conducted in the absence of any commercial or financial relationships that could be construed as a potential conflict of interest.

DATA AVAILABILITY STATEMENT

The data that support the findings of this study are available from the corresponding author upon reasonable request.

ORCID

Eva Smorodina https://orcid.org/0000-0002-5457-5163
Birgit Strodel https://orcid.org/0000-0002-8734-7765

REFERENCES

1. Hardy JA, Higgins GA. Alzheimer's disease: the amyloid cascade hypothesis. *Science*. 1992;256(5054):184-185.
2. Hardy J, Selkoe DJ. The amyloid hypothesis of Alzheimer's disease: progress and problems on the road to therapeutics. *Science*. 2002; 297(5580):353-356.
3. Hardy J. The discovery of Alzheimer-causing mutations in the APP gene and the formulation of the "amyloid cascade hypothesis". *FEBS J*. 2017;284(7):1040-1044.
4. Doig AJ. Positive feedback loops in Alzheimer's disease: the Alzheimer's feedback hypothesis. *J Alzheimers Dis*. 2018;66(1):25-36.
5. Tomski SJ, Murphy RM. Kinetics of aggregation of synthetic β-amyloid peptide. *Arch Biochem Biophys*. 1992;294(2):630-638.
6. Burgoyne RD, Helassa N, McCue HV, Haynes LP. Calcium sensors in neuronal function and dysfunction. *Cold Spring Harb Perspect Biol*. 2019;11(5):a035154.
7. Yu XM, Groveman BR, Fang XQ, Lin SX. The role of intracellular sodium (Na^+) in the regulation of calcium (Ca^{2+})-mediated signaling and toxicity. *Health*. 2010;2(1):8-15.
8. Slutsky I, Sadeghpour S, Li B, Liu G. Enhancement of synaptic plasticity through chronically reduced Ca2+ flux during uncorrelated activity. *Neuron*. 2004;44(5):835-849.
9. Andrási E, Páli N, Molnár Z, Kösel S. Brain aluminum, magnesium and phosphorus contents of control and Alzheimer-diseased patients. *J Alzheimers Dis*. 2005;7(4):273-284.
10. Nguyen PH, Ramamoorthy A, Sahoo BR, et al. Amyloid oligomers: a joint experimental/computational perspective on Alzheimer's disease, Parkinson's disease, type II diabetes, and amyotrophic lateral sclerosis. *Chem Rev*. 2021;121(4):2545-2647.
11. Paul A, Samantray S, Anteghini M, Khaled M, Strodel B. Thermodynamics and kinetics of the amyloid-β peptide revealed by Markov state models based on MD data in agreement with experiment. *Chem Sci*. 2021;12:6652-6669.
12. Balbach JJ, Ishii Y, Antzutkin ON, et al. Amyloid fibril formation by $A\beta_{16-22}$, a seven-residue fragment of the Alzheimer's β-amyloid peptide, and structural characterization by solid state NMR. *Biochemistry*. 2000;39(45):13748-13759.
13. Samantray S, Yin F, Kav B, Strodel B. Different force fields give rise to different amyloid aggregation pathways in molecular dynamics simulations. *J Chem Inf Model*. 2020;60(12):6462-6475.
14. Kav B, Strodel B. Does the inclusion of electronic polarisability lead to a better modelling of peptide aggregation? *RSC Adv*. 2022;12: 20829-20837.
15. Man VH, He X, Derreumaux P, et al. Effects of all-atom molecular mechanics force fields on amyloid peptide assembly: the case of $A\beta_{16-22}$ dimer. *J Chem Theory Comput*. 2019;15(2):1440-1452.
16. Illig AM, Strodel B. Performance of Markov state models and transition networks on characterizing amyloid aggregation pathways from MD data. *J Chem Theory Comput*. 2020;16(12):7825-7839.
17. Nguyen PH, Li MS, Derreumaux P. Effects of all-atom force fields on amyloid oligomerization: replica exchange molecular dynamics simulations of the Aβ 16–22 dimer and trimer. *Phys Chem Chem Phys*. 2011; 13(20):9778-9788.
18. Carballo-Pacheco M, Ismail AE, Strodel B. On the applicability of force fields to study the aggregation of amyloidogenic peptides using molecular dynamics simulations. *J Chem Theory Comput*. 2018;14: 6063-6075.
19. Samantray S, Schumann W, Illig AM, et al. *Molecular Dynamics Simulations of Protein Aggregation: Protocols for Simulation Setup and Analysis with Markov State Models and Transition Networks*. Springer US; 2022: 235-279.
20. Robustelli P, Piana S, Shaw DE. Developing a molecular dynamics force field for both folded and disordered protein states. *Proc Natl Acad Sci USA*. 2018;115(21):E4758-E4766.
21. Senguen FT, Doran TM, Anderson EA, Nilsson BL. Clarifying the influence of core amino acid hydrophobicity, secondary structure propensity, and molecular volume on amyloid-β 16-22 self-assembly. *Mol Biosyst*. 2011;7(2):497-510.
22. Mamatkulov S, Schwierz N. Force fields for monovalent and divalent metal cations in TIP3P water based on thermodynamic and kinetic properties. *J Chem Phys*. 2018;148(7):74504.
23. Aqvist J. Ion-water interaction potentials derived from free energy perturbation simulations. *J Phys Chem*. 1990;94(21):8021-8024.
24. Dang LX. Mechanism and thermodynamics of ion selectivity in aqueous solutions of 18-crown-6 ether: a molecular dynamics study. *J Am Chem Soc*. 1995;117(26):6954-6960.
25. Cheatham TE, Crowley MF, Fox T, Kollman PA. A molecular level picture of the stabilization of A-DNA in mixed ethanol–water solutions. *Proc Natl Acad Sci USA*. 1997;94(18):9626-9630.
26. Joung IS, Cheatham TE III. Determination of alkali and halide monovalent ion parameters for use in explicitly solvated biomolecular simulations. *J Phys Chem B*. 2008;112(30):9020-9041.
27. Joung IS, Cheatham TE III. Molecular dynamics simulations of the dynamic and energetic properties of alkali and halide ions using water-model-specific ion parameters. *J Phys Chem B*. 2009;113(40): 13279-13290.
28. Beglov D, Roux B. Finite representation of an infinite bulk system: solvent boundary potential for computer simulations. *J Chem Phys*. 1994;100(12):9050-9063.
29. Huang J, Rauscher S, Nawrocki G, et al. CHARMM36m: an improved force field for folded and intrinsically disordered proteins. *Nat Methods*. 2017;14(1):71-73.
30. Kirby BJ, Jungwirth P. Charge scaling manifesto: a way of reconciling the inherently macroscopic and microscopic natures of molecular simulations. *J Phys Chem Lett*. 2019;10(23):7531-7536.

31. Leontyev I, Stuchebrukhov A. Electronic continuum model for molecular dynamics simulations. *J Chem Phys*. 2009;130(8):2B609.

32. Leontyev I, Stuchebrukhov A. Electronic polarizability and the effective pair potentials of water. *J Chem Theory Comput*. 2010;6(10):3153-3161.

33. Leontyev IV, Stuchebrukhov A. Electronic continuum model for molecular dynamics simulations of biological molecules. *J Chem Theory Comput*. 2010;6(5):1498-1508.

34. Leontyev I, Stuchebrukhov A. Accounting for electronic polarization in non-polarizable force fields. *Phys Chem Chem Phys*. 2011;13(7):2613-2626.

35. Leontyev IV, Stuchebrukhov AA. Polarizable molecular interactions in condensed phase and their equivalent nonpolarizable models. *J Chem Phys*. 2014;141(1):06B621_1.

36. Benavides A, Portillo M, Chamorro V, Espinosa J, Abascal J, Vega C. A potential model for sodium chloride solutions based on the TIP4P/2005 water model. *J Chem Phys*. 2017;147(10):104501.

37. Zeron I, Abascal J, Vega C. A force field of Li^+, Na^+, K^+, Mg^{2+}, Ca^{2+}, Cl^-, and SO_4^{2-} in aqueous solution based on the TIP4P/2005 water model and scaled charges for the ions. *J Chem Phys*. 2019;151(13):134504.

38. Berendsen HJ, Postma J, Gunsteren vWF, DiNola A, Haak JR. Molecular dynamics with coupling to an external bath. *J Chem Phys*. 1984;81(8):3684-3690.

39. Bussi G, Donadio D, Parrinello M. Canonical sampling through velocity rescaling. *J Chem Phys*. 2007;126(1):14101.

40. Parrinello M, Rahman A. Polymorphic transitions in single crystals: a new molecular dynamics method. *J Appl Phys*. 1981;52(12):7182-7190.

41. Hess B, Bekker H, Berendsen HJ, Fraaije JG. LINCS: a linear constraint solver for molecular simulations. *J Comput Chem*. 1997;18(12):1463-1472.

42. Miyamoto S, Kollman PA. Settle: an analytical version of the SHAKE and RATTLE algorithm for rigid water models. *J Comput Chem*. 1992;13(8):952-962.

43. Essmann U, Perera L, Berkowitz ML, Darden T, Lee H, Pedersen LG. A smooth particle mesh Ewald method. *J Chem Phys*. 1995;103(19):8577-8593.

44. Van Der Spoel D, Lindahl E, Hess B, Groenhof G, Mark AE, Berendsen HJ. GROMACS: fast, flexible, and free. *J Comput Chem*. 2005;26(16):1701-1718.

45. Pronk S, Páll S, Schulz R, et al. GROMACS 4.5: a high-throughput and highly parallel open source molecular simulation toolkit. *Bioinformatics*. 2013;29(7):845-854.

46. Páll S, Abraham MJ, Kutzner C, Hess B, Lindahl E. Tackling exascale software challenges in molecular dynamics simulations with GROMACS. *Lecture Notes in Computer Science*. Springer; 2014:3-27.

47. Abraham MJ, Murtola T, Schulz R, et al. GROMACS: high performance molecular simulations through multi-level parallelism from laptops to supercomputers. *SoftwareX*. 2015;1:19-25.

48. McGibbon RT, Beauchamp KA, Harrigan MP, et al. MDTraj: a modern open library for the analysis of molecular dynamics trajectories. *Biophys J*. 2015;109(8):1528-1532.

49. Schäffler M, Khaled M, Strodel B. ATRANET–automated generation of transition networks for the structural characterization of intrinsically disordered proteins. *Methods*. 2022;206:18-26.

50. Daura X, Gademann K, Jaun B, Seebach D, Van Gunsteren WF, Mark AE. Peptide folding: when simulation meets experiment. *Angew Chem Int ed*. 1999;38(1–2):236-240.

51. Vögeli B, Ying J, Grishaev A, Bax A. Limits on variations in protein backbone dynamics from precise measurements of scalar couplings. *J Am Chem Soc*. 2007;129(30):9377-9385.

52. Wirmer J, Schwalbe H. Angular dependence of 1 J (N i, Cαi) and 2 J (N i, Cα(i-1)) coupling constants measured in J-modulated HSQCs. *J Biomol NMR*. 2002;23(1):47-55.

53. Viet MH, Ngo ST, Lam NS, Li MS. Inhibition of aggregation of amyloid peptides by beta-sheet breaker peptides and their binding affinity. *J Phys Chem B*. 2011;115(22):7433-7446.

54. Barz B, Wales DJ, Strodel B. A kinetic approach to the sequence–aggregation relationship in disease-related protein assembly. *J Phys Chem B*. 2014;118(4):1003-1011.

55. Bastian M, Heymann S, Jacomy M. Gephi: an open source software for exploring and manipulating networks. *Proc Int AAAI Conf Weblogs Soc Media*. 2009;3:361-362.

56. Smith MD, Cruz L. Changes to the structure and dynamics in mutations of Aβ21–30 caused by ions in solution. *J Phys Chem B*. 2013;117(48):14907-14915.

57. Smith MD, Cruz L. Effect of ionic aqueous environments on the structure and dynamics of the Aβ21–30 fragment: a molecular-dynamics study. *J Phys Chem B*. 2013;117(22):6614-6624.

58. Jalali S, Yang Y, Mahmoudinobar F, Singh SM, Nilsson BL, Dias C. Using all-atom simulations in explicit solvent to study aggregation of amphipathic peptides into amyloid-like fibrils. *J Mol Liq*. 2022;347:118283.

59. Yamazaki M, Ikeda K, Kameda T, Nakao H, Nakano M. Kinetic mechanism of amyloid-β-(16–22) peptide fibrillation. *J Phys Chem Lett*. 2022;13(26):6031-6036.

60. Schäffler M, Samantray S, Strodel B. Transition networks unveil disorder-to-order transformations in Aβ caused by glycosaminoglycans or lipids. *Int J Mol Sci*. 2023;24:11238.

61. Iannuzzi C, Irace G, Sirangelo I. The effect of glycosaminoglycans (GAGs) on amyloid aggregation and toxicity. *Molecules*. 2015;20(2):2510-2528.

62. Gallardo R, Ranson NA, Radford SE. Amyloid structures: much more than just a cross-β fold. *Curr Opin Struct Biol*. 2020;60:7-16.

63. Willbold D, Strodel B, Schröder GF, Hoyer W, Heise H. Amyloid-type protein aggregation and prion-like properties of amyloids. *Chem Rev*. 2021;121(13):8285-8307.